Investigation of Fe and Ni-based alloys as highly-active and low-cost oxygen evolution reaction catalyst in alkaline media

Lucile Magnier [1,2], Garance Cossard [2], Vincent Martin [2], Céline Pascal [1], Virginie Roche [2], Eric Sibert [2], Irina Shchedrina [3], Richard Bousquet [4], Valérie Parry [1], Marian Chatenet [2]

[1] Univ. Grenoble Alpes, CNRS, Grenoble INP (Institute of Engineering, Univ. Grenoble Alpes), SIMAP, F-38000 Grenoble, France
[2] Univ. Grenoble Alpes, Univ. Savoie Mont Blanc, CNRS, Grenoble INP (Institute of Engineering, Univ. Grenoble Alpes), LEPMI, 38000 Grenoble, France
[3] Pierre Chevenard Research Center, APERAM Alloys Imphy, 58160, Imphy, France
[4] Product Development, APERAM Alloys Imphy, 58160, Imphy, France
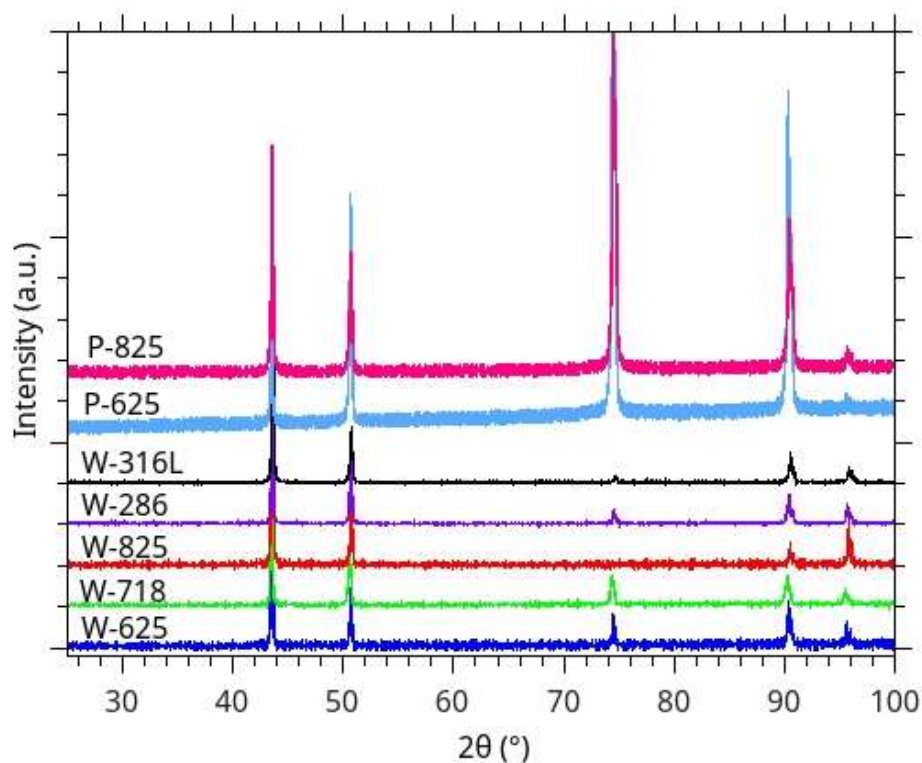
Figure S1: XRD in Bragg-Brentano geometry of the initial state on wires (W -) and plates (P -) after polishing. The change in peak relative intensity between wires and plates evidences different preferential grain orientations.

The chemical composition of the various alloys was characterized by SEM-EDS to determine the near-surface composition of the as-received materials; because these alloys underwent various surface treatments (hot rolling, pickling), the composition of the first tens of microns may differ from a mean bulk composition. The local composition of the materials (at the as-received state) was evaluated because it may drive their electrochemical behavior. The measured values by SEM-EDS are however fully compared to the (bulk) data from APERAM (alloy supplier). The two sets of measurements agree within ±4%, which is reasonable assuming the accuracy of semi-quantitative SEM-EDS analyses.

Table S1: Alloy chemical compositions in major elements in at.% determined using SEM-EDS (error determined from the analysis of four 0.45 mm^2 zones), compared with Aperam data sheets.

| at. %		Fe	Ni	Cr	Mo	Nb	Other addition elements	Fe/Ni
W-316L	SEM-EDS	70.50 ± 0.04	9.53 ± 0.07	17.68 ± 0.07	1.19 ± 0.01	-	Mn, Si, Al	7.40
	APERAM	71.2	7.6	19.4	1.8	-	-	9.4
W-286	SEM-EDS	55.6 ± 0.1	22.8 ± 0.1	15.8 ± 0.1	0.674 ± 0.005	-	Ti, Mn, Al, Si, V	2.44
	APERAM	55.4	23.5	15.3	0.7	-	Ti, Mn, Al, V, Si	2.36
W-825	SEM-EDS	35.3 ± 0.2	36.6 ± 0.3	23.4 ± 0.3	1.45 ± 0.01	-	Cu, Ti, Al, Si, Mn	0.97
	APERAM	34.9	37.1	23.1	1.6	-	Cu, Ti, Mn, Si	0.94
P-825	SEM-EDS	33.17 ± 0.09	34.2 ± 0.2	26.5 ± 0.1	0.98 ± 0.02	-	Cu, Ti, Si, Mn, Al	0.97
	APERAM	32.8	37.1	24.2	1.7	-	Cu, Ti, Si, Mn	0.88
W-718	SEM-EDS	21.76 ± 0.08	50.8 ± 0.1	19.95 ± 0.07	1.79 ± 0.03	3.14 ± 0.05	Ti, Al, Mn, Si	0.43
	APERAM	20.7	52.1	20.0	1.8	3.1	Ti, Al	0.40
W-625	SEM-EDS	0.3 ± 0.1	65.6 ± 0.3	25.9 ± 0.2	5.08 ± 0.09	2.34 ± 0.09	Al, Ti	0.005
	APERAM	0.3	65.9	25.5	5.4	2.3	Al, Ti, Si, Mn	0.005
P-625	SEM-EDS	0.27 ± 0.01	64.7 ± 0.6	29.0 ± 0.5	3.23 ± 0.07	1.51 ± 0.03	Al, Ti, Si, Mn	0.004
	APERAM	0.3	65.9	25.2	5.6	2.3	Al, Ti, Si, Mn	0.005
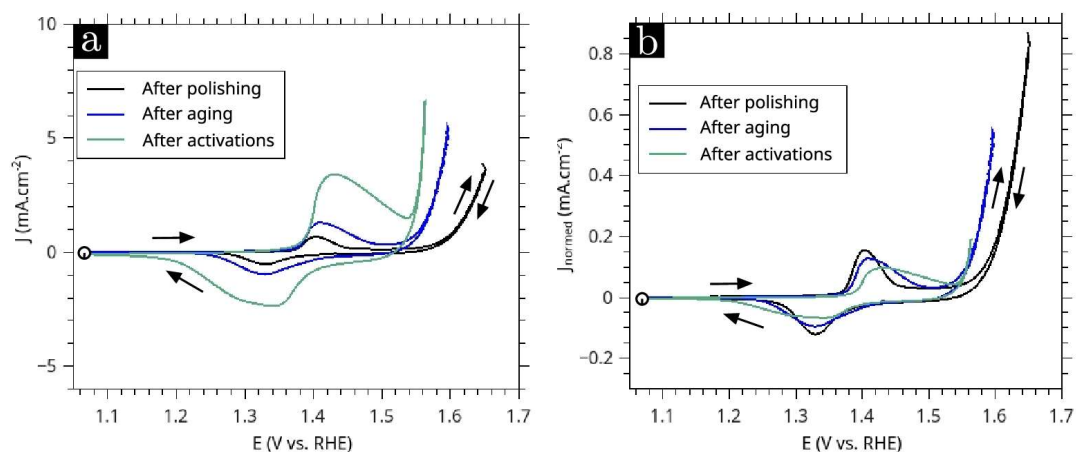
Supplementary Figure S2: Electrochemical characterization of P-625: (a) CV scans performed at 50 mV.s^{-1}, (b) CV scans normalized by the Ni^{III}/Ni^{II} reaction capacity (reported in Fig. 1f). The start of the CVs is indicated by the dot and the scan direction by the arrows.
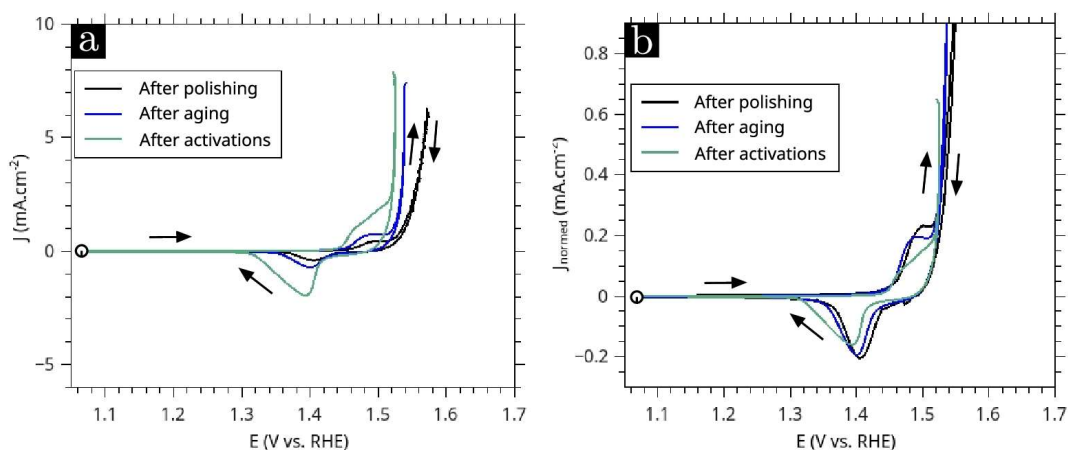
Supplementary Figure S3: Electrochemical characterization of P-825: (a) CV scans performed at 50 mV.s^{-1}, (b) CV scans normalized by the Ni^{III}/Ni^{II} reaction capacity (reported in Fig. 1f). The start of the CVs is indicated by the dot and the scan direction by the arrows.
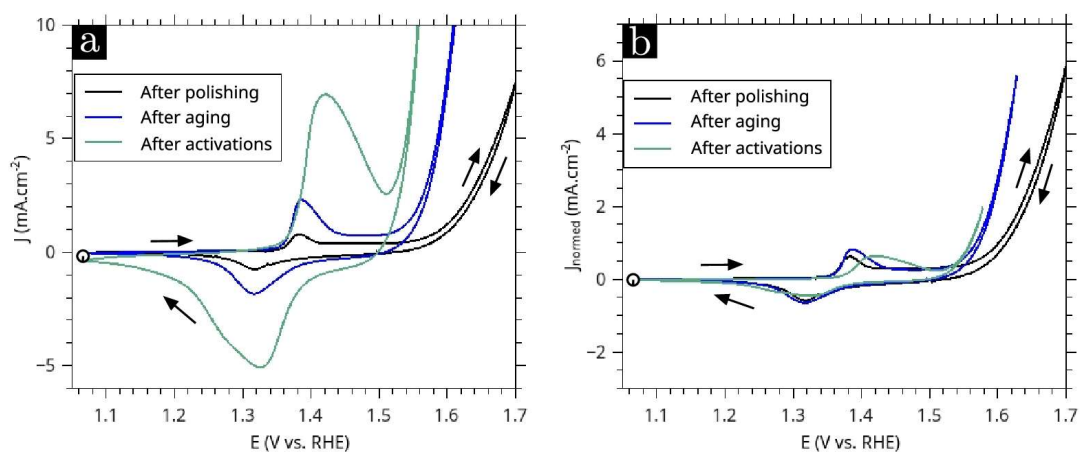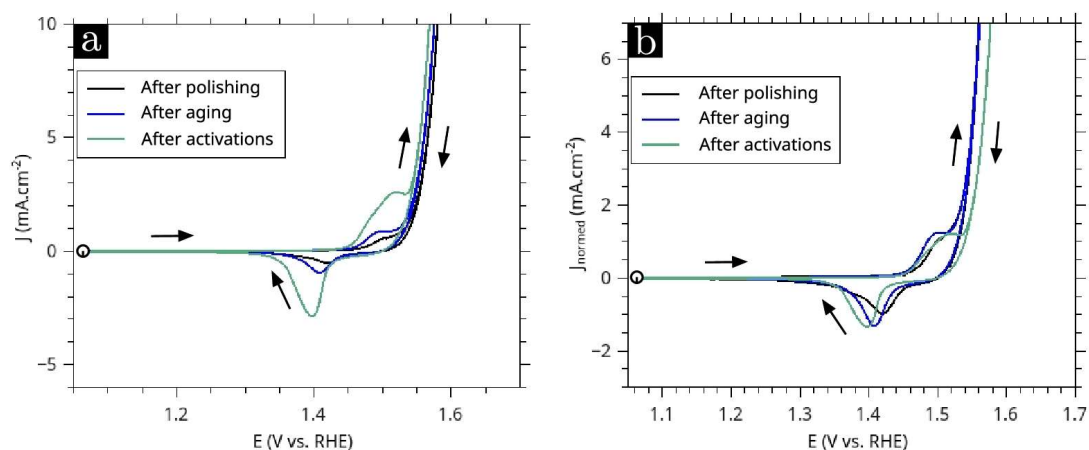

Supplementary Figure S4: Electrochemical characterization of W-625: (a) CV scans performed at 50 mV.s^{-1}, (b) CV scans normalized by the Ni^{III}/Ni^{II} reaction capacity (reported in Fig. 1f). The start of the CVs is indicated by the dot and the scan direction by the arrows.
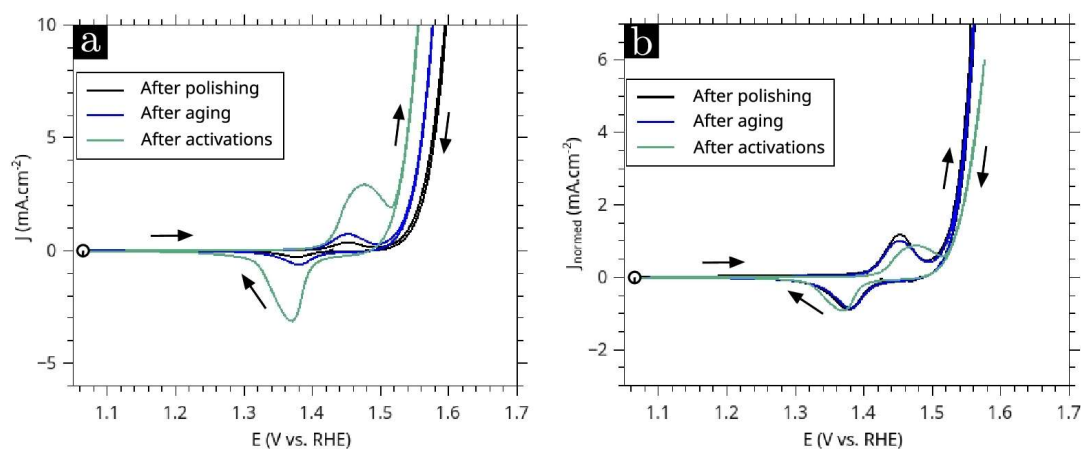
Supplementary Figure S5: Electrochemical characterization of W-718: (a) CV scans performed at 50 mV.s^{-1}, (b) CV scans normalized by the Ni^{III}/Ni^{II} reaction capacity (reported in Fig. 1f). The start of the CVs is indicated by the dot and the scan direction by the arrows.
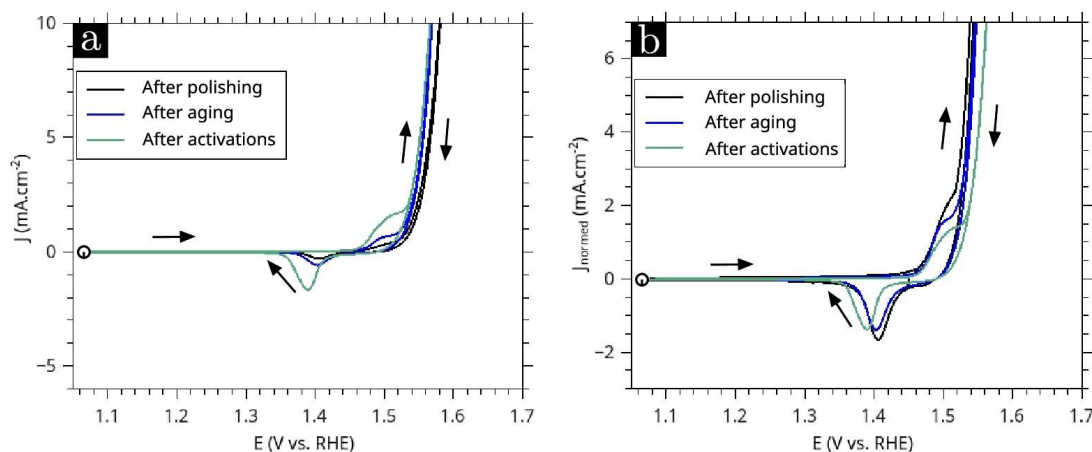
Supplementary Figure S6: Electrochemical characterization of W-825: (a) CV scans performed at 50 mV.s^{-1}, (b) CV scans normalized by the Ni^{III}/Ni^{II} reaction capacity (reported in Fig. 1f). The start of the CVs is indicated by the dot and the scan direction by the arrows.
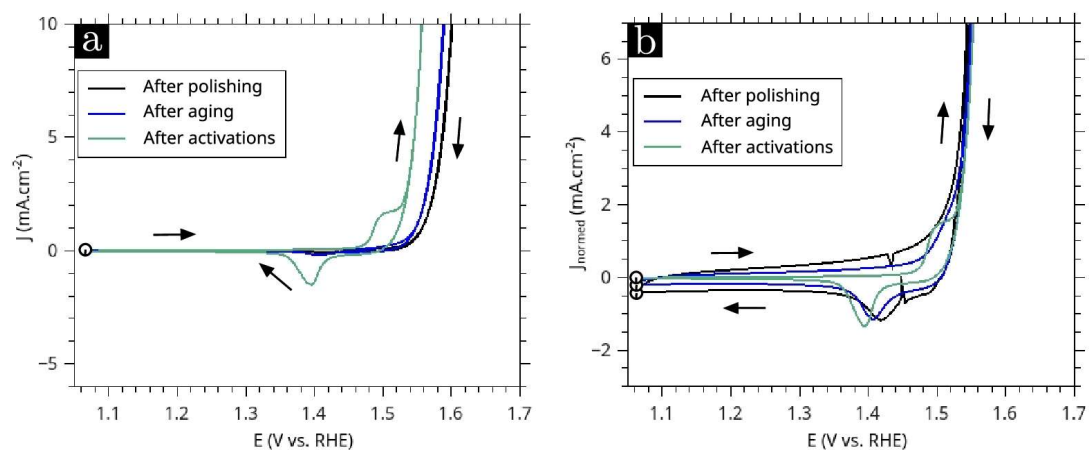

Supplementary Figure S7: Electrochemical characterization of W-286: (a) CV scans performed at 50 mV.s^{-1}, (b) CV scans normalized by the Ni^{III}/Ni^{II} reaction capacity (reported in Fig. 1f). The start of the CVs is indicated by the dot and the scan direction by the arrows.

Supplementary Figure S8: Electrochemical characterization of W-316L: (a) CV scans performed at 50 mV.s^{-1}, (b) CV scans normalized by the Ni^{III}/Ni^{II} reaction capacity (reported in Fig. 1f). The start of the CVs is indicated by the dot and the scan direction by the arrows.
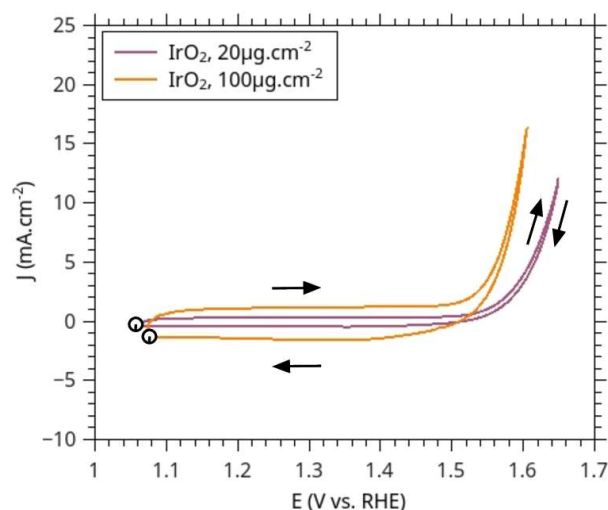
Supplementary Figure S9: Electrochemical characterization of IrO₂ with two loadings: 20 µg.cm⁻² and 100 µg.cm⁻². The CV scans are performed at 50 mV.s⁻¹. The start of the CVs is indicated by the dot and the scan direction by the arrows.

Figure S10.a shows the results of long-term (48 h) tests performed at J = 5 mA cm⁻² constant OER current density (2 replicates have been made for W-718 and W-625, and 3 replicates for W-825). In such conditions, all materials slowly lose activity, while during the activations (alternation of high/low potentials, *i.e.* mimicking the operation of an alkaline electrolyser directly coupled to intermittent sources of electricity) the activity kept increasing. This clearly demonstrates that such Ni-Fe alloys are more robust for practical (non-stationary) application than for stationary one, and confirms findings from Chung *et al.* [1] that the Fe-doped Ni-oxohydroxide sites are dynamically stable. It also confirms the findings of Todoroki *et al.* [2] specifying that the OER activity is better maintained upon potential alternation than at fixed potential/current. Harsher protocol of degradation was then applied (Figure S10.b-g): fast-scan CV, applied between 0.5 and 1.8 V vs RHE at 1 V.s⁻¹, according to the procedure of Todoroki *et al.* [3] and Fujita *et al.* [4]. The potential measured at 5 mA.cm⁻² (b, d, f) and at 10 mA.cm⁻² (c, e, g) after such accelerated stress test (After AST), show that all surfaces have improved OER activity versus their pristine state (After polishing). Surfaces initially rich in Fe further activate After AST versus After activations, which is not the case for the Fe-poor W-625 surface. This peculiar behavior agrees with the results of Todoroki *et al.*, which showed that pure Ni surfaces do not improve after such harsh AST, on the contrary to 316L and other alloys of the Austenitic stainless-steel family) [3].
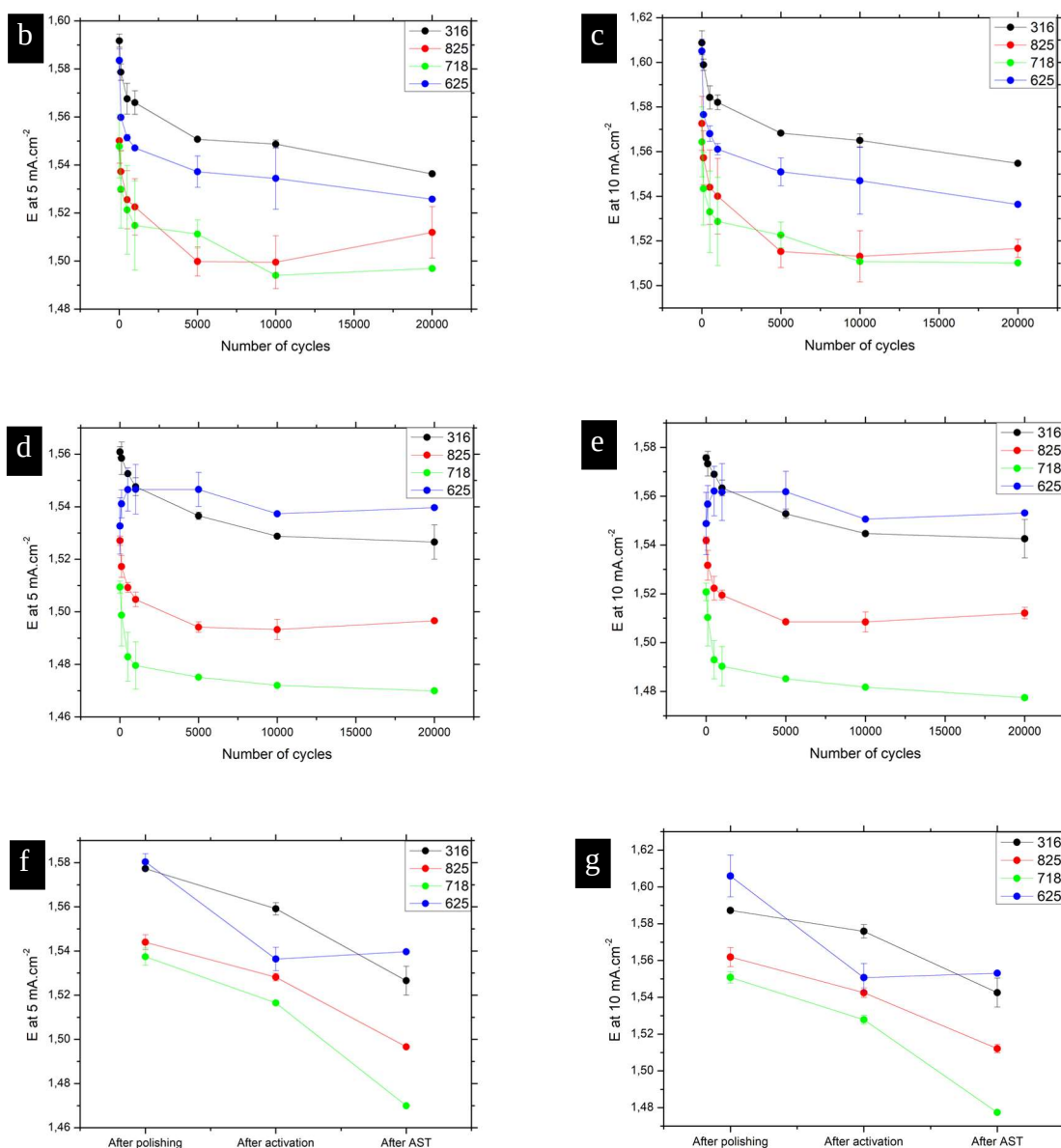

5
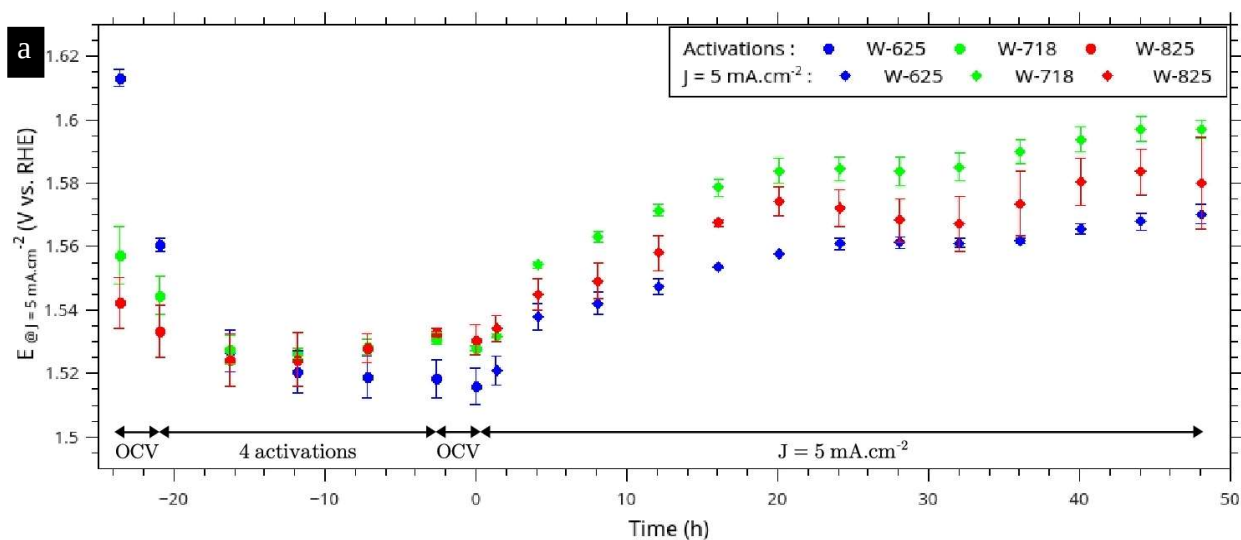
Figure S10: Durability tests on the Fe-Ni alloys. (a) Evolution of the OER performance of the W-625, W-718 and W-825 alloys upon constant polarization at J = 5 mA.cm^{-2}. The negative time corresponds to the activation process investigated along the manuscript: the OER potential (at J = 5 mA.cm^{-2}) decreases during OCV and activations. During the positive time (48 h), a constant OER current density (5 mA.cm^{-2}) is imposed and the corresponding potential is reported on the figure. (b-g) Evolution of the OER performance measured at the W-316, W-625, W-718 and W-825 alloys during a CV plotted between 0.5 and 1.65 V vs RHE at 20 mV.s^{-1} in 0.1 M KOH at 25°C, along the AST performed in the same electrolyte (fast-scan CV, applied between 0.5 and 1.8 V vs RHE at 1 V.s^{-1}, according to the procedure of Todoroki et al. [3] and Fujita et al. [4]. OER potential measured at (b) 5 mA.cm^{-2} and (b) 10 mA.cm^{-2} for the initially polished surfaces, and at (c) 5 mA.cm^{-2} and (d) 10 mA.cm^{-2} for the initially activated surfaces (see main text for precision on the activation procedure). Graphs (f) and (g) compare the OER activities of each surface in its pristine state (After polishing), after 11 cycles of activation (After activations) and after 20 000 cycles of AST (After AST). In any case, the error bars reflect the standard deviations of the measurements, that have been reproduced at least 2 and maximum 6 times (usually 4 times), depending on the number of cycles of AST considered.

These results demonstrate, in a very clear and reproducible manner, that all the Fe-Ni alloys evaluated here are robust, hence suitable, for application under potential fluctuations. This further confirms the long-term stability of the prepared electrodes and is likely related to the better stability of active layers formed by exsolution versus layers deposited on the substrate [5].

Supplementary Figure S11.a plots the OER potential of W-625 after three polishing states: (i) full polishing until OPU colloidal silica suspension, (ii) partial polishing stopped after the 1 μm diamond suspension and (iii) after the P2400 SiC abrasive paper (medium diameter 6.5 μm). In the main text, "after polishing" corresponds in this figure to the "OPU" samples (full polishing until OPU colloidal silica suspension), the other polishing states being tested only in this study. The roughness of the metal/electrolyte interface does not affect the overall trends and only slightly modifies the OER potential values. Moreover, absence of polishing was characterized using plates, whose electrochemically tested surface is directly the rolled surface: Supplementary Figure S11.b shows that the absence of polishing does not deteriorate the OER performance; on the contrary, the OER potentials are lower.
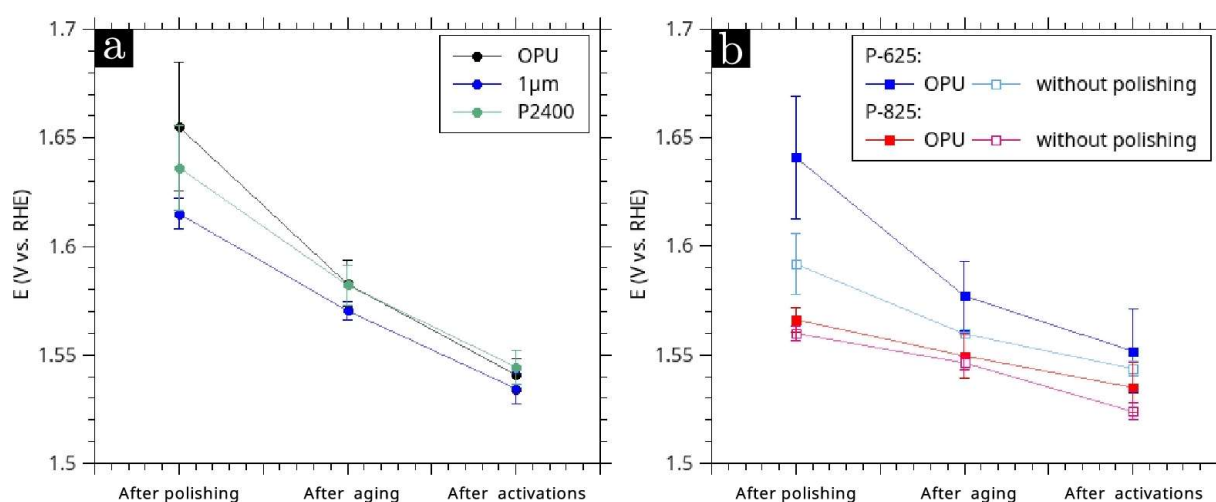
Supplementary Figure S11: Influence of the sample surface state. (a) Study of the influence of the last polishing step on the W-625 grade. (b) Comparison of the plates with the full polishing until OPU colloidal silica suspension ("OPU") with the processed plates ("without polishing"). Potentials are measured at a current density of 5 mA.cm^{-2}.

The faradaic efficiency (FE) of OER was evaluated for our Fe-Ni alloys, to stress whether OER is the dominant process (or not).

Firstly, rotating ring-disk evaluation has been achieved, by slightly adapting the procedure of Chung *et al.* [1] (see materials and method section in the main text).
In any case, the H$_2$O$_2$ detection was insignificant, showing that the water oxidation at the Fe-Ni alloys is essentially the 4-electrons OER (as reported in [1]). The detection of O$_2$ evolved at the disk is close to 100% for all the Fe-Ni alloys, should it be in initial state (right after polishing and before any electrochemical activation) or after 1 to 11 activations (Figure S12). Only the initial region where an oxidation current is monitored on the OER CV is not well reproduced by the corrected ring current, and this is due to (i) the possible oxidation/dissolution of metals into cations when the active layer forms [and this essentially applies in the first positive cycle of voltamperometry, *i.e.* before the first activation] and (ii) the capacitive behaviour of the Fe-doped Ni-oxohydroxide surface (Ni^{II} to Ni^{III} transition) [which progressively grows upon the activation - see Fig. S13]. In any case, in the region of large oxidation currents of the OER CVs, the disk and ring-corrected currents near-perfectly superpose, showing that the O$_2$ evolution is the very dominant reaction at that stage. This shows that the FE is close to 100%, once the active layer has been formed on the Fe-Ni alloy surface, which is nearly achieved within one positive scan for the alloys tested here.
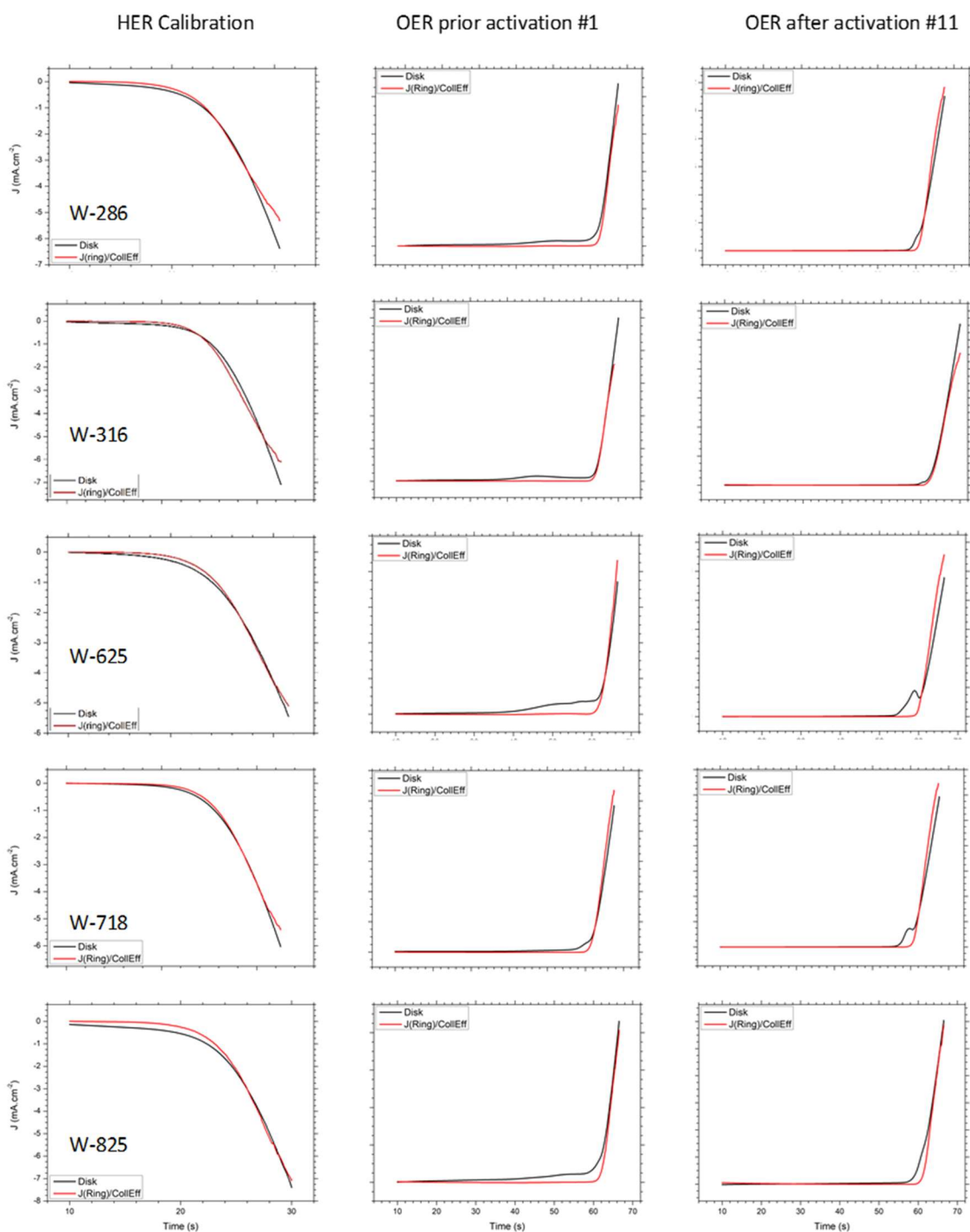
Figure S12: Example of HER calibration and OER faradaic measurements for the Fe-Ni alloys (W-286, W-316L, W-625, W-718 and W-825). In any case, the disk HER current (left column) or OER currents measured prior activation #1 and after activation #11 (middle and right column, respectively) are displayed in black (Disk), while the corrected ring currents are displayed in red (J(Ring)/CollEff). The experimental collection efficiency of a given electrode was adjusted so that the HER disk current matches with the measured ring current; then, the same value of collection efficiency was applied to the ring current in all the OER experiments.

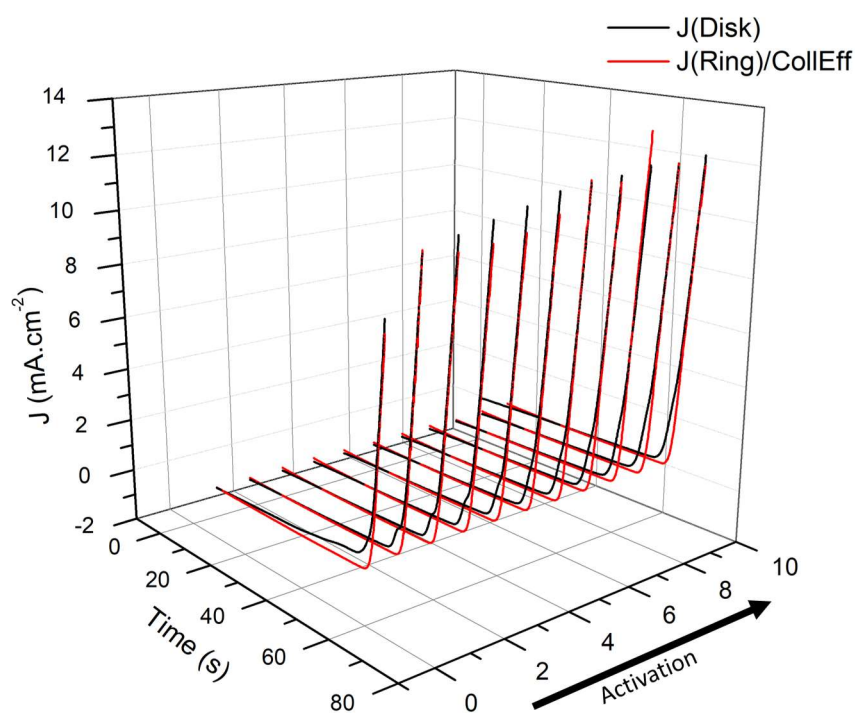Figure S13: Evolution of the OER current at the disk and O_2 detection at the ring for the W-825 alloy in function of the number of activations. In any case, the disk OER currents are displayed in black, while the corrected ring currents of O_2 detection are displayed in red (J(Ring)/CollEff). The collection efficiency of the electrode was kept constant from the initial value of the HER calibration.

Figure S13 shows how the OER current at the disk and O_2 detection at the ring vary for the W-825 alloy as a function of the number of activations. The activation progressively results in larger OER currents at the disk and the O_2 detection at the ring remains near-perfect in the course of the experiment. In particular (at the foot of the OER regime), the "mismatch" between the disk oxidation current and the O_2 detection at the ring evolves: in the first activation, this mismatch start "early" (lower values of potential), owing to the slight but irreversible dissolution of unstable components of the bulk alloy (here Cr, Mo, Ni, Fe, etc.), leading to the formation of the Fe-doped Ni-oxohydroxide layer (see main text). Once this layer is formed (at larger potential values), the disk oxidation current is (very) well reproduced by the O_2 detection at the ring (after correction by the collection efficiency). In the second cycle (after the first activation), the early mismatch essentially disappears, and only a shoulder right before the OER regime maintains, which correspond to the capacitive behaviour of the Fe-doped Ni-oxohydroxide surface (Ni^{II} to Ni^{III} transition) and progressively grows upon the activation, as the oxides layer becomes thicker.

Secondly, elemental analyses of the used electrolytes have been achieved by ICP-MS after a sequence of (i) OER characterizations, (ii) aging at OCV and then (iii) OER characterizations for the W-625, W-718 and W-825 electrodes; the OER characterizations consisted of 11 cycles from 1.061 to 1.761 V vs RHE at 50 mV.s^{-1}, performed before and after the 2.5 h of OCV. The electrolyte (0.1 M KOH) is used to calibrate the ICP-MS measurements, so the concentrations reported in Table S2 correspond to the variations with respect to the initial electrolyte (ion dissolution in the electrolyte). The results show that metal leaching is very low (ppb level in the electrolyte), in agreement with the composition of the very thin Fe-doped NiOOH layers detected on the alloys surface by TEM-EDS (Figs. 2-3) and analyzed by XPS: only Mo, Cr, Ti, Cu and to some extent Nb and Ni are detected in the spent electrolyte. In particular, neither major Ni and Fe are detected, which shows that these components, if dissolving upon activations, do

essentially redeposit as Fe-doped NiOOH at the surface of the base metal. As a matter of fact, only traces are detected for Fe, which seems to indicate that Fe redeposition (from the Fe contained in the unpurified electrolyte) was prevalent versus Fe dissolution upon the tested OER conditions.

Table S2: ICP-MS analyses of the 0.1 M KOH electrolyte after a sequence of (i) OER characterizations, (ii) aging at OCV and then (iii) OER characterizations of the W-625, W-718 and W-825 electrodes. The concentrations are given in ppb and the error bar for the measurements is below 10%. $Q_{m, metal}$ is the maximum coulometry corresponding to the metal electrodissolution, assuming the number of electrons considered per ion and the composition of the solution. $Q_{ox, total}$ is the oxidation charge measured in the whole electrochemical procedure (22 cycles of CV, related to OER + possible metal electrodissolution). The faradaic efficiency of OER is calculated from these two values: FE = 100 ($Q_{ox, total}$ - $Q_{m, metal}$)/$Q_{ox, total}$

	W-625	W-718	W-825	Number of electrons considered per ion
Al / ppb	Traces	Traces	Traces	3
Nb / ppb	0.2	0.6	0.1	5
Ni / ppb	0.2	0.4	0.2	3
Cr / ppb	2.5	1.0	0.8	3
Mo / ppb	12.2	10.1	11.8	4
Ti / ppb	0.6	0.2	0.7	4
Cu / ppb	0.6	0.03	1.0	2
Fe / ppb	Traces	Traces	Traces	3
$Q_{m, metal}$ / mC	2.95	2.14	2.51	
$Q_{ox, total}$ / mC	219	409	375	
FE / %	**98.6**	**99.5**	**99.3**	

From these values, assuming the maximum number of electrons per metal ion in solution (right column of Table S2), the total coulometry corresponding to the metal electrodissolution $Q_{m, metal}$ was calculated. Comparing this value to $Q_{ox, total}$ the oxidation charge measured in the whole electrochemical procedure (22 cycles, related to OER + possible metal electrodissolution), the faradaic efficiency of OER can be calculated: (FE) exceeds 98% for all alloys, in agreement with the RRDE data presented above. Note that this value is likely underestimated (for the ICP-MS dosing), as the coulometry of metal electrodissolution ($Q_{m, metal}$) also integrates the possible metal dissolution that occurred at OCV, a period during which there is of course not any oxidation charge to integrate.
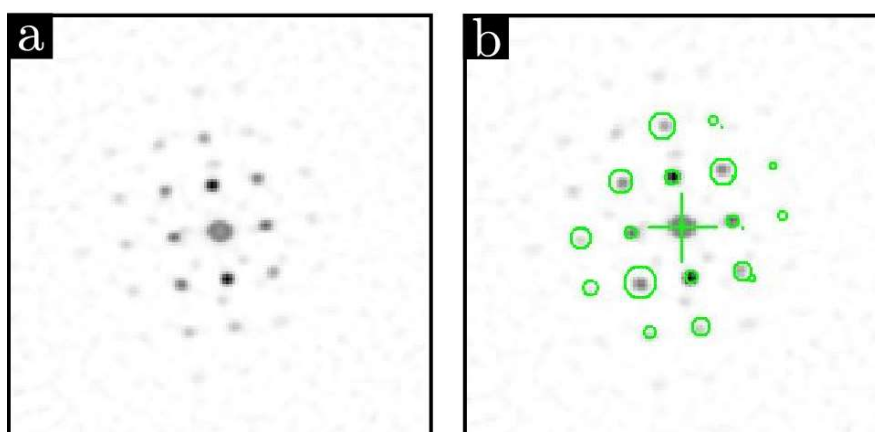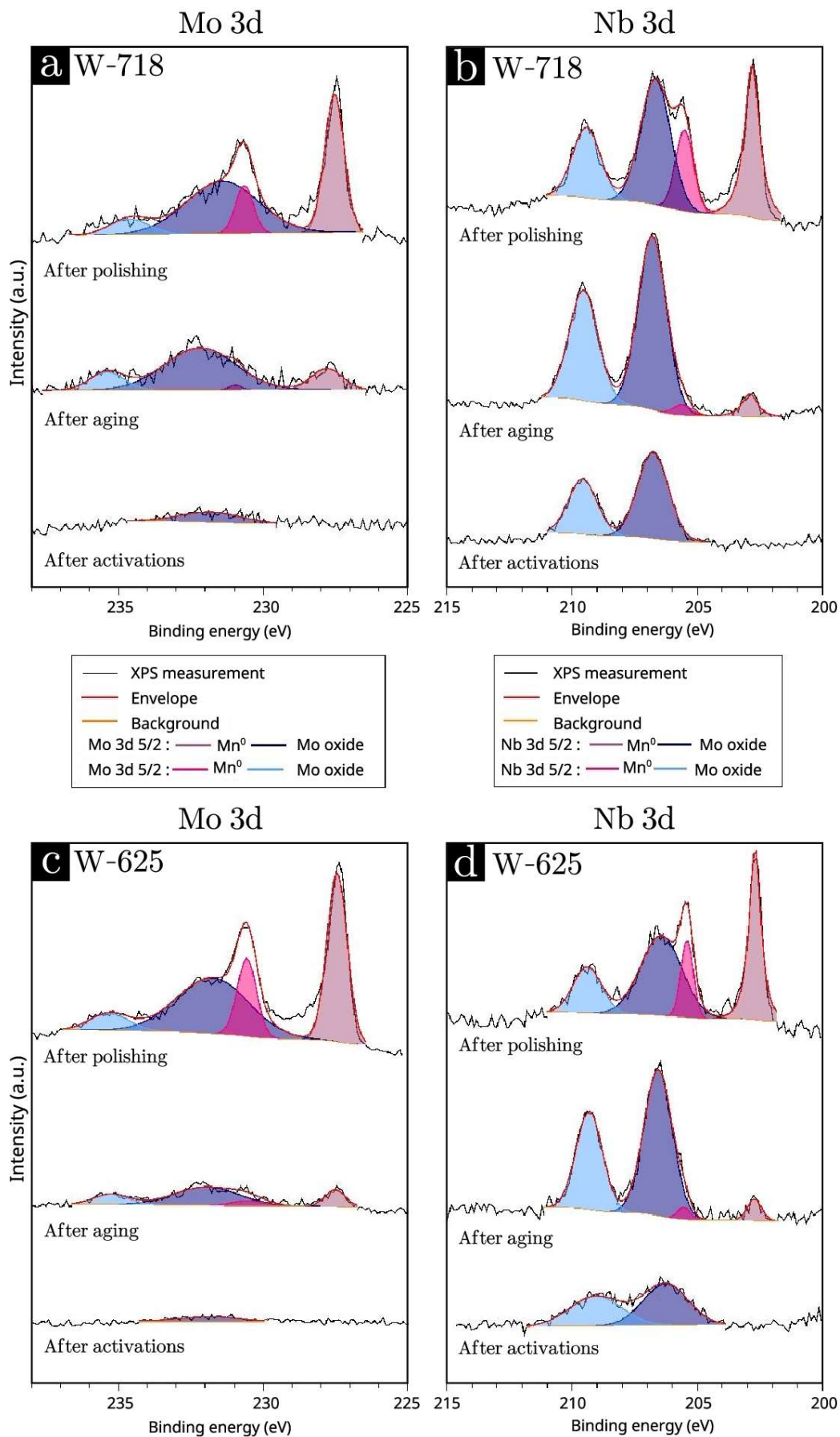

Figure S14: TEM analysis of W-718 after activations. (a) Diffraction pattern in a well crystallized zone in the active-surface layer. (b) Correspondence between the cubic NiO phase (green circles) and the diffraction pattern of (a).

Supplementary Figure S15: XPS analysis of W-718: (a) Mo 3d and (b) Nb 3d. XPS analysis of W-625: (c) Mo 3d and (d) Nb 3d. The fitting parameters used are reported in Tables S6 and S7. Three samples per grade were analyzed by XPS after polishing, aging and activations.

Tables S3 to S5 report the fitting parameters of XPS spectra of Fig. 4 (Ni 2p, Fe 2p, Fe 3p and Cr 2p). Tables S6 and S7 are the fitting parameters used to fit Mo 3d and Nb 3d XPS spectra (Fig. S15).

Table S3: XPS Ni peak fit parameters [6–8]

		E_b (eV)	FWHM (eV)
Ni 2p	Ni	852.6 ± 0.2	1.12 ± 0.05
	Ni sat	858.4 ± 0.2	3.2 ± 0.1
	NiO	853.7 ± 0.3	2.0 ± 0.2
	NiO doublet	855.7 ± 0.2	2.4 ± 0.6
	NiO sat	860.6 ± 0.3	3.8 ± 0.2
	Ni^{2+}/Ni^{3+}	855.8 ± 0.2	2.5 ± 0.3
	Ni^{2+}/Ni^{3+} sat	861.6 ± 0.2	3.0 ± 0.4

Table S4: XPS Fe peak fit parameters [9,10]

		E_b (eV)	FWHM (eV)
Fe 2p $^3/_2$	Fe^0	706.7 ± 0.1	0.9 ± 0.2
	Fe_2O_3	710.7 ± 0.2	2.6 ± 0.2
	FeOOH	712.7 ± 0.2	3.4 ± 0.2
Fe 2p $^1/_2$	Fe_2O_3	724.3 ± 0.1	2.4 ± 0.1
	FeOOH	726.2 ± 0.1	3.0 ± 0.1
Fe 3p	Fe_2O_3	55.4 ± 0.1	2.0 ± 0.1
	FeOOH	56.8 ± 0.1	2.3 ± 0.1

Table S5: XPS Cr peak fit parameters [7,10]

		E_b (eV)	FWHM (eV)
Cr 2p	Cr^0	573.6 ± 0.2	1.63 ± 0.05
	Cr_2O_3	575.9 ± 0.2	2.1 ± 0.2
	$Cr(OH)_3$	577.2 ± 0.4	2.6 ± 0.3

Table S6: XPS Mo peak fit parameters [11]

		E_b (eV)	FWHM (eV)
Mo 3d $^5/_2$	Mo^0	227.6 ± 0.2	0.8 ± 0.2
	Mo oxide	232.1 ± 0.3	2.5 ± 0.5
Mo 3d $^3/_2$	Mo^0	230.8 ± 0.3	0.6 ± 0.3
	Mo oxide	235.3 ± 0.3	1.5 ± 0.1

Table S7: XPS Nb peak fit parameters [11]

		E_b (eV)	FWHM (eV)
Nb 3d $^5/_2$	Nb^0	202.9 ± 0.3	0.8 ± 0.3
	Nb oxide	206.6 ± 0.2	1.6 ± 0.3
Nb 3d $^3/_2$	Nb^0	205.5 ± 0.1	0.7 ± 0.2
	Nb oxide	209.4 ± 0.2	1.5 ± 0.4

Surface-enrichment by migration of Fe contained in the bulk cannot be excluded. To discriminate between two origins (Fe migration from the bulk and Fe impurities contained in the electrolyte), a 99.999% pure Ni (W-Ni) sample was studied and characterized by SEM-EDS, XRD and electrochemical measurements (Table S8, Figs. S16 and S17). The OER potential of W-Ni is significantly reduced after aging and activations, alike W-625, while its Ni^{III}/Ni^{II} capacity and Ni active site efficiency (decrease of $E(J_{normed})$) both increase (Figs. S17b,d). Figure S17a reveals the positive shift of the Ni redox peaks, signing Fe incorporation, which explains the improved OER performances after aging and activations. The presence of impurity in the electrolyte (prepared from KOH pellets, 85%) is thus the origin of the Fe incorporation in the oxide layer.

The Pourbaix diagrams [12] for Fe, Ni, Cr, Mo and Nb clearly show that in OER conditions ($E> 1$ V vs RHE) in alkaline electrolytes (pH 13 or above), only Ni has stable solid phases: oxo-hydroxides; the other elements are stable in solution in the form of MO_4^{2-} anions. XPS confirms that, beside Fe (and of course Ni) that create Fe-doped NiOOH, the other elements are really present as traces in the oxide layer, therefore shall not develop so much active area. Hence, they shall not directly drive the OER performance. However, as specified in our contribution, their presence could help the formation of the oxide layer, and particularly its 3D-construction into larger amounts of active sites, hence indirectly driving the final OER activity.

Table S8: Details of the main characteristics of pure Ni (Alfa Aesar, 99.999%). The column "Commercial reference" is the Alfa Aesar reference and the column "Label" is the name that is used in this article to refer simply to the samples. The "Process" column gives the indication of the processing of the sample. The "Geometric surface" column is the active area tested electrochemically (used to calculate the current density). The chemical composition, determined by SEM-EDS, is given in atomic percent.

Commercial reference	Label	Process	Geometric surface (cm²)	SEM-EDS			
				Ni	Al	Si	Fe/Ni
Nickel rod 99.999%	W-Ni	Wire	0.2	99.8 ± 0.1	0.11 ± 0.03	0.10 ± 0.05	0
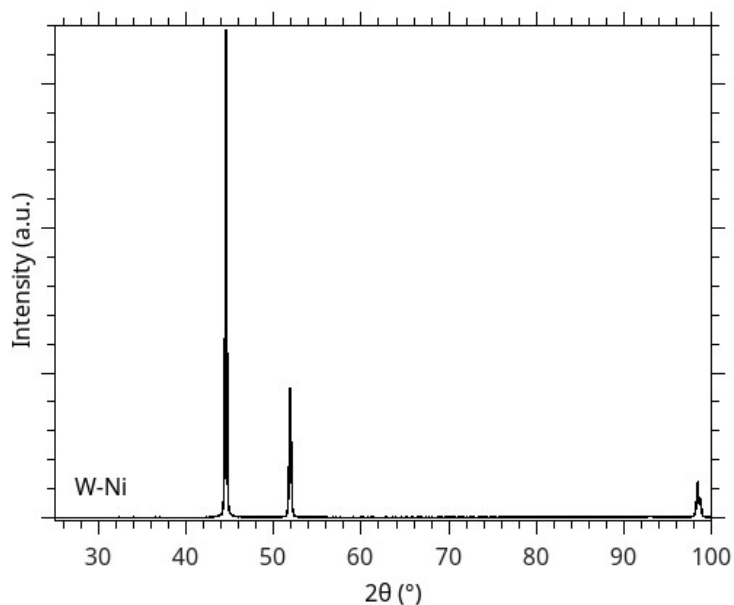
Supplementary Figure S16: XRD in Bragg-Brentano geometry of the initial state on W-Ni after polishing.
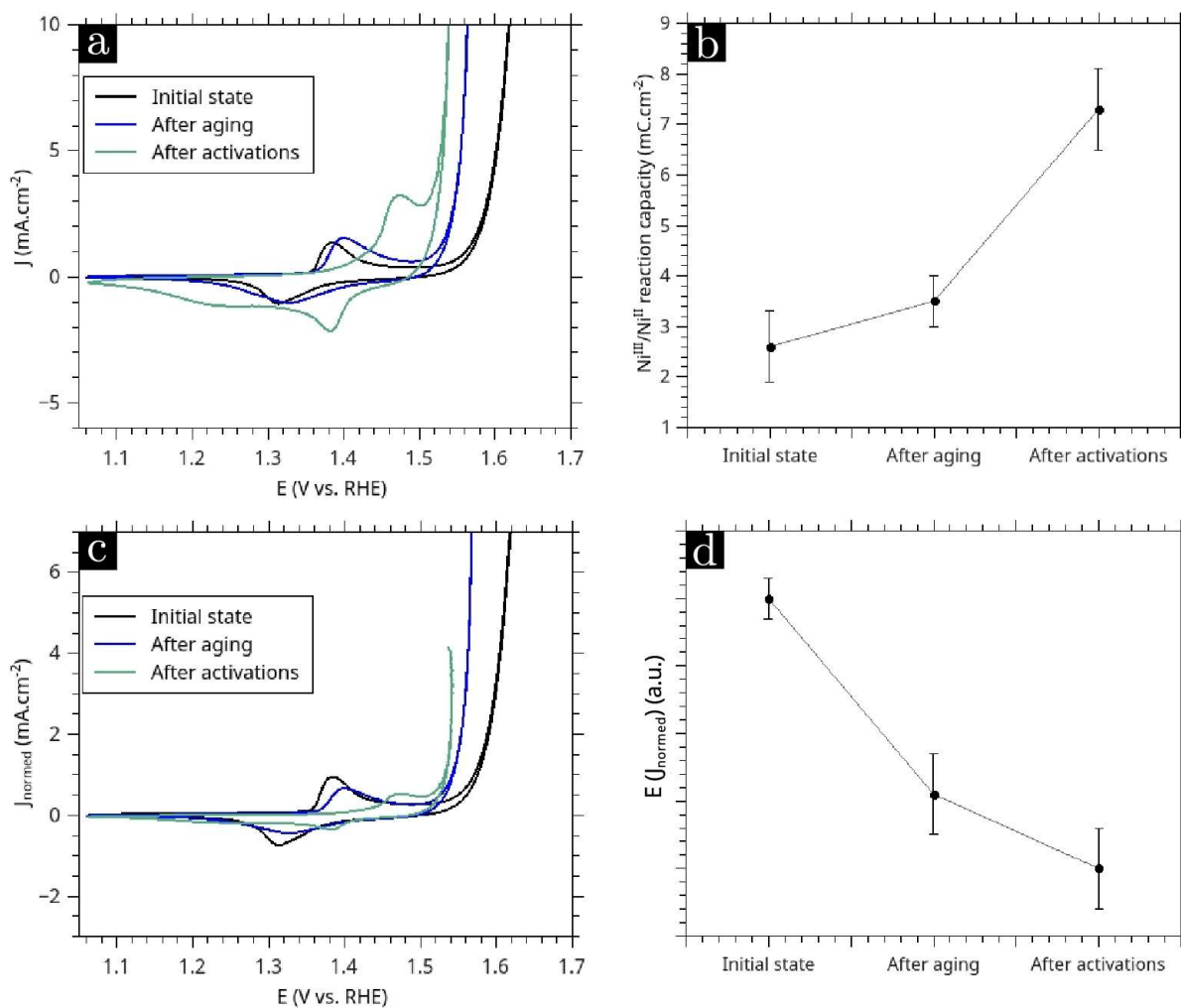
Supplementary Figure S17: Electrochemical characterization of W-Ni. (a) CV scans performed at 50 mV.s^{-1}. (b) Evolution of the Ni^{III}/Ni^{II} reaction capacity for each grade in the initial state, after aging and after activations. The value is calculated from the integration of the Ni^{III}/Ni^{II} reduction peaks of the CV scans in Fig. a. (c) CV scans normalized by the Ni^{III}/Ni^{II} reaction capacity (reported in Fig. b). (d) Evolution of the active site performance: a decrease in potential corresponds to an increase in active site performance. These values are extracted from Fig. c.

A sample of invar (W-Invar) was tested (Table S9). This grade is essentially composed of Fe and Ni, with a very low content of minor elements (Table S10). This grade also shows an austenitic structure according to XRD analysis (Fig. S18).

The electrochemical characteristics are plotted in Fig. S19. No improvement in OER performances occurs with aging and activations (Fig. S19a). Figure S19b reveals the very small evolution of the Ni^{III}/Ni^{II} reaction capacity. The decrease in active site performance (increase in potential for the same normalized current density) is displayed in Fig. S19d.

Table S9: Details of the main characteristics of W-Invar. The column "Commercial reference" is the Aperam reference and the column "Label" is the name that is used in this article to refer simply to the samples. The "Process" column gives the indication of the processing of the sample. The "Geometric surface" column is the active area tested electrochemically (used to calculate the current density).

Commercial reference	Label	Process	Geometric surface (cm²)
INVAR ®	W-Invar	Wire	0.246

Table S10: Chemical composition of W-Invar, determined by SEM-EDS, is given in atomic percent, compared with Aperam data sheets. NB: 0.1% is the detection limit of EDS quantification

	Fe	Ni	Si	Al	Mn	Cr	Fe/Ni
SEM-EDS	65.4 ± 0.1	34.1 ± 0.2	0.20 ± 0.02	< 0.1	< 0.1	< 0.1	1.92
APERAM	64.2	34.9	0.4	-	0.5	-	1.84
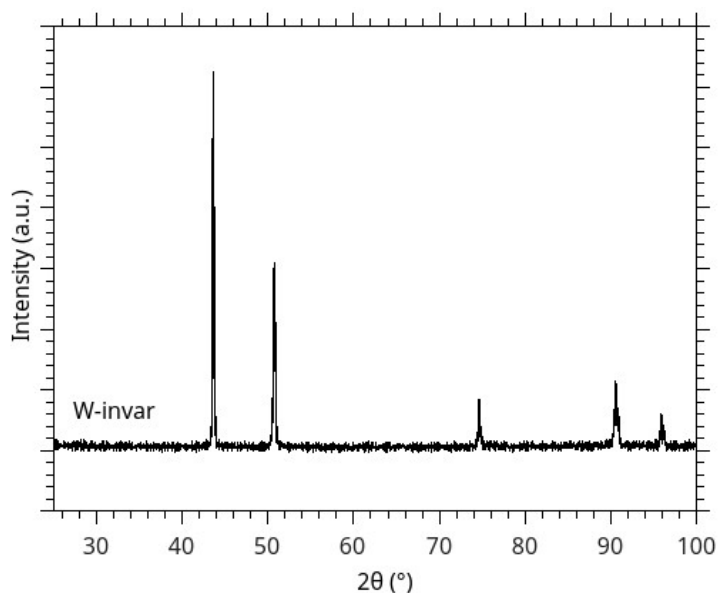
Supplementary Figure S18: XRD in Bragg-Brentano geometry of the initial state on W-Invar after polishing.
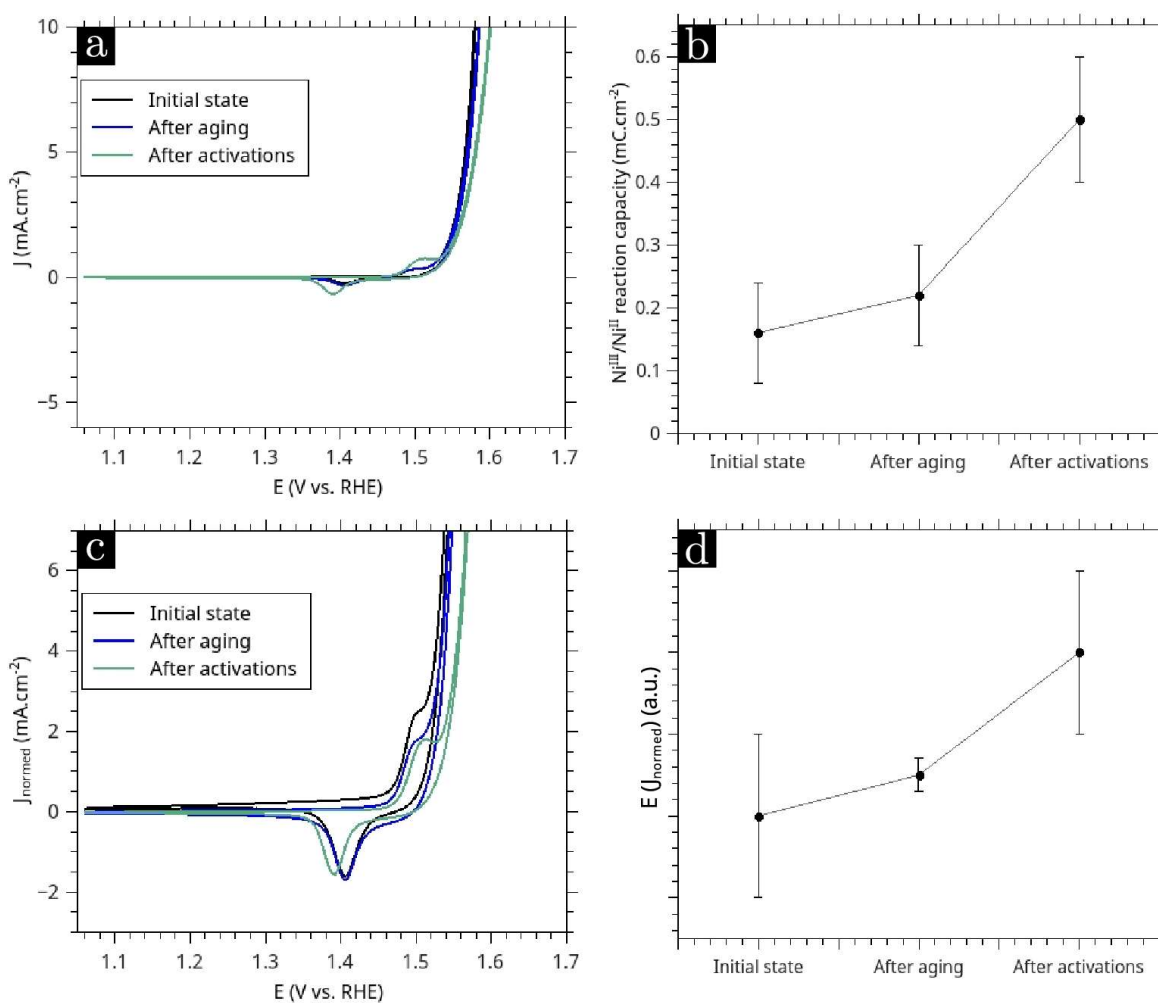
Supplementary Figure S19: Electrochemical characterization of W-Invar. (a) CV scans performed at 50 mV.s^{-1}. (b) Evolution of the Ni^{III}/Ni^{II} reaction capacity for each grade in the initial state, after aging and after activations. The value is calculated from the integration of the Ni^{III}/Ni^{II} reduction peaks of the CV scans in Fig. a. (c) CV scans normalized by the Ni^{III}/Ni^{II} reaction capacity (reported in Fig. b). (d) Evolution of the active site performance: a decrease in potential corresponds to an increase in active site performance. These values are extracted from Fig. c.
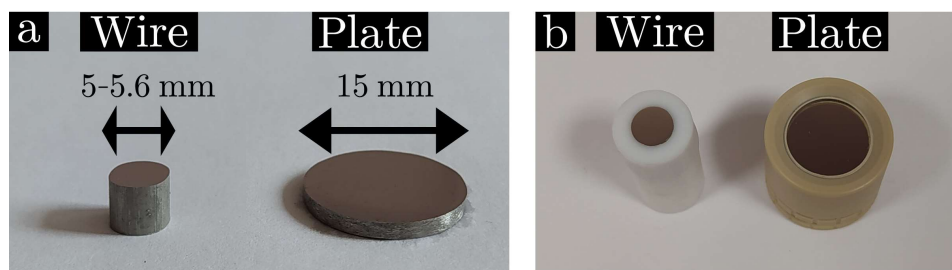
Supplementary Figure S20: Image of wires and plates: (a) after cutting, (b) placed in the sample holders.

The scan rate has a minimal impact on the potential measured at a current density of 5 mA cm^{-2} (one of the activity markers considered in this study, see Fig. S21); the potential only varies by a few mV depending on the scan rate, which overall denotes for the minimal impact of the potential scan rate with the kinetic markers chosen herein. This is ascribed to the fact that (i) only smooth polished surfaces were tested (this was deliberate, so to minimize the capacitive behaviour of the electrodes) and (ii) they display very high faradaic OER activity; as a result, the faradaic contribution overwhelms the capacitive one. 50 mV.s^{-1} was chosen (20 mV.s^{-1} in the RRDE experiments), so to limit as much as possible hindrance by the evolved oxygen bubbles, which becomes more prevalent at lower potential scan rate.
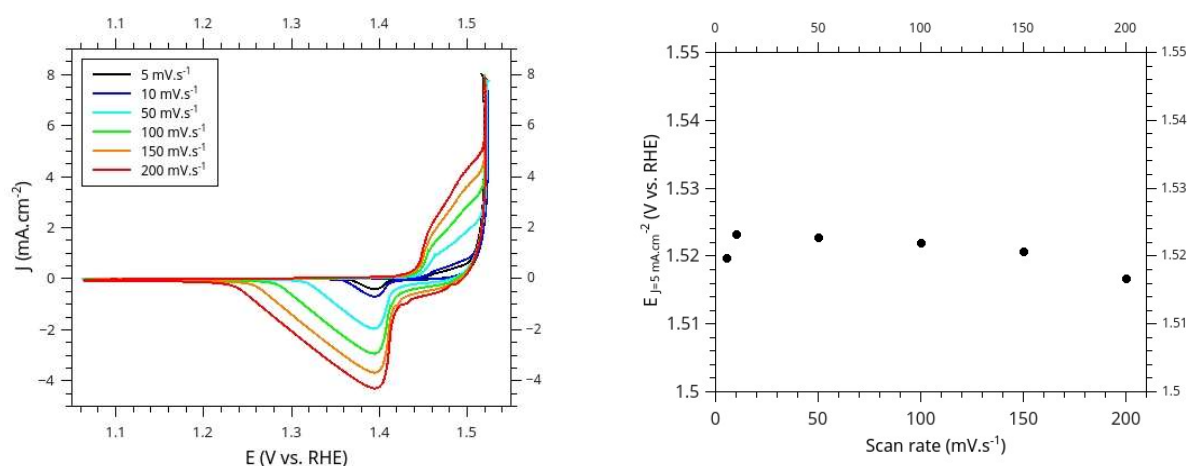
Supplementary Figure S21: (left) CV scan at different scan rates on P-825 after activations. (right) Potential at a current density of 5 mA.cm^{-2} reported from the CV scans at different scan rates.

References

[1] Chung, D. Y. et al. Dynamic stability of active sites in hydr (oxy) oxides for the oxygen evolution reaction. *Nature Energy* 5, 222-230 (2020)

[2] Todoroki, N. & Wadayama, T. Electrochemical stability of stainless-steel-made anode for alkaline water electrolysis: Surface catalyst nanostructures and oxygen evolution overpotentials under applying potential cycle loading. *Electrochemistry Communications* **122**, 106902 (2021)

[3] Todoroki, N. & Wadayama, T. Dissolution of constituent elements from various austenitic stainless steel oxygen evolution electrodes under potential cycle loadings. *International Journal of Hydrogen Energy.***47**, 32753-32762 (2022)

[4] Fujita, S. et al. The effect of Li$_x$Ni$_{2-x}$O$_2$/Ni with modification method on activity and durability of alkaline water electrolysis anode. *Electrocatalysis.***9**, 162-171 (2018)

[5] Neagu, D. et al. In situ observation of nanoparticle exsolution from perovskite oxides: from atomic scale mechanistic insight to nanostructure tailoring. *ACS nano.***13**, 12996-13005 (2019)

[6] Ali-Löytty, H. et al. Ambient-pressure XPS study of a Ni–Fe electrocatalyst for the oxygen evolution reaction. *J. Phys. Chem. C.***120**, 2247–2253 (2016)

[7] Biesinger, M. C. et al. Resolving surface chemical states in XPS analysis of first row transition metals, oxides and hydroxides: Cr, Mn, Fe, Co and Ni. *Appl. Surf. Sci.***257**, 2717–2730 (2011)

[8] Todoroki, N. et al. Nanostructures and oxygen evolution overpotentials of surface catalyst layers synthesized on various austenitic stainless steel electrodes. *Electrocatalysis.***13**, 116–125 (2022)

[9] McIntyre, N. S. & Zetaruk, D. G. X-ray photoelectron spectroscopic studies of iron oxides. *Anal. Chem.***49**, 1521–1529 (1977)

[10]   Asami, K. & Hashimoto, K. The X-ray photo-electron spectra of several oxides of iron and chromium. *Corros. Sci.***17**, 559–570 (1977)

[11]   Chastain, J. & King Jr, R. C. Handbook of X-ray photoelectron spectroscopy. *Perkin-Elmer Corp.***40** (1992)

[12] Pourbaix, M. *Atlas of Electrochemical Equilibria in Aqueous Solutions*, National Association of Corrosion Engineers, Houston, 1979.